



UNIVERSITY OF LEEDS

This is a repository copy of *Microstructures reveal multistage melt present strain localisation in mid-ocean gabbros*.

White Rose Research Online URL for this paper:
<https://eprints.whiterose.ac.uk/161340/>

Version: Accepted Version

Article:

Gardner, RL, Piazzolo, S orcid.org/0000-0001-7723-8170, Daczko, NR et al. (1 more author) (2020) Microstructures reveal multistage melt present strain localisation in mid-ocean gabbros. *Lithos*, 366-367. 105572. ISSN 0024-4937

<https://doi.org/10.1016/j.lithos.2020.105572>

© 2020 Elsevier B.V. Licensed under the Creative Commons Attribution-NonCommercial-NoDerivatives 4.0 International License (<http://creativecommons.org/licenses/by-nc-nd/4.0/>).

Reuse

This article is distributed under the terms of the Creative Commons Attribution-NonCommercial-NoDerivatives (CC BY-NC-ND) licence. This licence only allows you to download this work and share it with others as long as you credit the authors, but you can't change the article in any way or use it commercially. More information and the full terms of the licence here: <https://creativecommons.org/licenses/>

Takedown

If you consider content in White Rose Research Online to be in breach of UK law, please notify us by emailing eprints@whiterose.ac.uk including the URL of the record and the reason for the withdrawal request.



eprints@whiterose.ac.uk
<https://eprints.whiterose.ac.uk/>

1 Microstructures reveal multistage melt 2 present strain localisation in mid-ocean 3 gabbros

4 *Robyn L. Gardner¹, Sandra Piazzolo², *Nathan R. Daczko¹ Patrick Trimby^{3,4}*

5 ¹Australian Research Council Centre of Excellence for Core to Crust Fluid Systems/GEMOC,
6 Department of Earth and Environmental Sciences, Macquarie University, NSW 2109, Australia.

7 ²School of Earth and Environment, University of Leeds, Leeds LS2 9JT, United Kingdom

8 ³Australian Centre for Microscopy and Microanalysis, University of Sydney, NSW 2006, Australia

9 ⁴Oxford Instruments, High Wycombe HP123SE, United Kingdom

10

11 *corresponding author: robyn.gardner@mq.edu.au Phone: 61-2-9850 8371

12 **Abstract**

13 In this work, we examine the tectono-metamorphic evolution of gabbroic rocks of the Atlantis Bank
14 oceanic core complex, South West Indian Ridge, focusing on multistage strain localisation associated
15 with exhumation. We study a sample from the core complex footwall below the depth of seawater
16 hydrothermal fluid-rock interaction. We identify a succession of increasing strain localisation where
17 early solid-state deformation of an olivine gabbro is succeeded by two episodes of melt present
18 deformation resulting in increasing localisation of both strain and melt flux into a narrowing zone.

19 The early melt-absent solid-state deformation occurs dominantly in the dislocation creep regime,
20 and localises strain at the tens of metre scale. This evolved into melt present deformation
21 characterised by grain size reduction by replacement reactions and dislocation creep and incipient
22 grain boundary sliding in coarse- and fine-grained parts, respectively. This is based on (1)
23 microstructures indicative of the former presence of melt, (2) a shift to lower calcium plagioclase,
24 and (3) reaction textures involving partial replacement of olivine and diopside by fine grained
25 enstatite and hornblende exhibiting only minor internal deformation features.

26 A narrow (2–3 mm) high strain zone which cuts the earlier shear zone foliation at $\sim 30^\circ$, exhibits
27 strong and near complete grain size reduction by melt-rock reaction and tightly spaced foliation
28 within a millimetre-wide high strain zone. Here, strain localisation is contemporaneous with a
29 second melt influx shown by (1) complete olivine replacement by fine grained hornblende and
30 enstatite exhibiting no crystallographic preferred orientation (2) microstructures indicative of the
31 former presence of melt and (3) changes in the mineral chemistry of diopside, plagioclase, enstatite
32 and hornblende. We suggest deformation was dominated by melt assisted grain boundary sliding
33 allowing higher volumes of melt flux, a high degree of weakening and deformation focused in the
34 narrow shear zone than during the porous melt flow in the wider, early shear zone.

35 This combined microstructural and microchemical study highlights that the recognition of changes in
36 deformation regime, their time relationships and potential melt related deformation are critical for
37 understanding, and therefore modelling, progressive strain localisation, melt flux and the rheological
38 evolution of oceanic detachment faults.

39

40

41 **Highlights:**

- 42 • Evolution from diffuse to localised deformation
- 43 • Microstructures indicate the former presence of melt within shear zones
- 44 • Melt flux causes melt-rock reactions, grain size reduction & strain localisation
- 45 • Evidence of multiple fluxes of external melt associated with strain localisation
- 46 • Positive feedback of melt flux, strain localisation and rheological weakening

47 **Keywords:**

48 Scientific ocean drilling; oceanic core complex; strain localisation; melt microstructures; melt-
49 present deformation.

50 **1. Introduction**

51 Research over the last five decades has shown that oceanic crust can exhibit significant strain
52 localisation at both plate boundaries and within the plates. One of the most important features of
53 strain localisation recognised in oceanic crust are detachment faults associated with core complexes.
54 These complexes are domal structures formed by kilometre-scale exhumation on a detachment fault
55 that evolved from ductile to brittle conditions. Consequently, strain localisation is a fundamental
56 requirement for core complex formation (Karson, 1999; Tucholke et al., 1998; Whitney et al., 2013
57 and references therein). Importantly, sites of strain localisation are associated with focused fluid
58 pathways that are significant for economic mineralisation (e.g. Eisenlohr et al., 1989 and references
59 therein).

60 Oceanic core complexes have been studied at mid ocean ridges with slow and very slow (e.g. Atlantis
61 Bank, South West Indian Ridge, Dick et al., 1999a) spreading rates. Previous conceptual and
62 numerical models stress the relative importance of magma supply rate and/or rheological

63 weakening in the evolution of strain localisation in the core-related detachment system (Buck et al.,
64 2005; Howell et al., 2019; Olive et al., 2010; Whitney et al., 2013 and references therein).

65 Rheological weakening and therefore strain localisation can be facilitated by a number of processes
66 including (1) brittle failure (Gardner et al., 2015 and references therein), (2) grain size reduction
67 (Bürgmann and Dresen, 2008; Rybacki and Dresen, 2004), (3) reaction softening (Hobbs et al., 2010;
68 White and Knipe, 1978 and references therein), (4) switch in deformation mechanism (Rybacki and
69 Dresen, 2004; Smith et al., 2015), (5) phase mixing (Cyprych et al., 2016; Ji et al., 2001), (6) thermal
70 softening triggered by exothermic metamorphic reactions and/or shear heating (Brodie and Rutter,
71 1987; Hobbs et al., 2008), and/or (7) the presence of a free fluid phase, e.g. melt (Renner et al., 2000
72 and references therein).

73 In general, there are two main deformation regimes observed at elevated temperatures and low to
74 intermediate stress (Etheridge and Wilkie, 1979), resulting in distinct changes of the stress exponent
75 (usually n) in stress-strain equations. The last decades of microstructural work has shown that
76 different microstructural characteristics can be linked to these regimes. (Regime 1) Dislocation creep
77 ($n > 3$) is grain size independent and is characterised by the movement of dislocations through the
78 mineral lattice causing grain size reduction by sub-grain formation and rotation, bulging and
79 nucleation. Internal deformation of the grains and the development of a crystallographic preferred
80 orientation (CPO) is a marker for dislocation creep. Dislocation creep is typical of the solid-state
81 deformation recognised in many natural shear zones (Urai et al., 1986). (Regime 2) Diffusion creep
82 ($n = 1$) is grain size dependent and is characterised by the movement of vacancies and is favoured
83 where grain size is small. The microstructural markers are no internal deformation within individual
84 grains, no CPO and no necking of the shear zone, but with a shape preferred orientation. One
85 feature of this process is the apparent movement of grains passed each other, often termed grain
86 boundary sliding. Over the last decade, it has become clear that there is an intermediate regime,
87 where grain boundary sliding is accommodated by dislocation glide ($n \sim 2$) (Hansen et al., 2011). A

88 single mineral type can undergo different processes depending on the grain size and location of the
89 grains, and these processes can change as the deformation continues (e.g. Svahnberg and Piazzolo,
90 2010). Recent work shows that grain boundary sliding can occur without a clear accommodating
91 process resulting in the generation of a dynamic porosity (Fusseis et al., 2009; Menegon et al., 2015).
92 In this case, the n value is between 1 and 2 and fluid may flux through the system. Furthermore, if
93 melt is present, melt may reduce the strength of the deforming rock by several orders of magnitude
94 (Rosenberg and Handy, 2005). The exact reason for this is still under debate, however melt presence
95 as films along grain boundaries may be a key factor (e.g. Stuart et al., 2018b).

96 Even though, detailed microstructural and microchemical analysis is necessary to recognize the
97 deformation regimes and different processes of localisation, the long-lived and continuous nature of
98 sequentially lower grade tectono-metamorphism in evolving oceanic core complexes has to some
99 extent hampered the interpretation of the relative timing and/or coeval nature of deformation and
100 melt/fluid-rock interactions in such systems. To date there are relatively few detailed
101 microstructural examinations of gabbroic oceanic drill cores have been undertaken, exceptions being
102 Mehl and Hirth (2008) and Miranda and John (2010), and no study has examined the potential
103 impact of melt migration during deformation in such settings. Features such as the common spatial
104 association of oxides with areas of deformation in oceanic gabbroic rocks (Dick et al., 1999b) remain
105 unexplained. In this work we focus on a sample taken from the Ocean Drilling Program (ODP) Leg
106 176 core 735B in the Atlantis Bank oceanic core complex, Southwest Indian Ridge (SWIR), a very slow
107 spreading ridge. In order to study the evolution of strain localisation and weakening processes
108 during the formation of oceanic core complexes, we chose to investigate a sample from the ODP
109 core at 953.7 meters below seafloor (mbsf) from the detachment footwall in order to assess the
110 potential significance of melt flux in the deformation of these rocks. The sample was chosen to be
111 well below the zone of seawater hydrothermal alteration as asserted by the work of Gao et al.
112 (2006) who examined $\delta^{18}\text{O}$ in olivine, clinopyroxene and plagioclase to be from 0–800 mbsf.
113 Interestingly, Gao et al. (2007) determined, using rare earth elements (REEs) in clinopyroxene at 880

114 mbsf that at this depth samples did not interact with seawater, but instead the REE variability
115 resulted from melt-rock interaction. This supports earlier work by Gillis and Meyer (2001) who
116 found, using hornblende compositions from the top 500m of the core that the REEs and
117 temperatures were consistent with a magmatic rather than an hydrothermal origin for the hydration
118 reaction textures that formed hornblende.

119 Although the gabbroic rocks from >800 mbsf lack hydrothermal alteration, they are still strongly
120 heterogeneous (Dick et al., 2000). The gabbros are variably deformed, have diverse geochemistry
121 and display complex melt-rock reaction textures. High strain zones have been previously interpreted
122 to have localised in near-solidus gabbro, while still a crystal mush (Cannat, 1991; Dick et al., 2002) or
123 solid state conditions by dislocation creep and local diffusion creep (Mehl and Hirth, 2008). Bloomer
124 et al. (1991) suggest highly fractionated interstitial liquid of the oxide-poor gabbro locally
125 accumulated into these elongate zones of deformation to form most oxide gabbro bodies; i.e., oxide
126 gabbro bodies are genetically and spatially related to their host gabbro.

127 We use detailed microstructural and mineral chemistry analyses to identify weakening processes
128 that controlled the history of strain localisation of these rocks. We recognise that the evolution of
129 strain localisation began with dynamic recrystallisation during melt/fluid-absent solid-state, crystal
130 plastic deformation. Initial rheological weakening is enhanced by flux of an externally derived melt
131 by deformation-assisted porous melt flow (e.g. Meek et al., 2019) within dynamically recrystallised
132 zones where melt-rock reactions result in further reduced grain size creating a positive feedback that
133 further localised strain and melt flux. At least two syntectonic, either episodic or continuous, melt
134 flux events can be recognized. Based on our interpretation of progressive strain localisation, we
135 suggest that in addition to solid state deformation, infiltration of melt and weakening due to melt-
136 present deformation are important processes in the evolution of oceanic core complexes, and that
137 melt-present deformation is potentially under-recognised in oceanic rocks.

138 **2. Atlantis Bank oceanic core complex**

139 The Atlantis Bank oceanic core complex is situated south east of Africa on the ultra-slow spreading
140 Southwest Indian Ridge (SWIR). Atlantis Bank is a ridge 720m below the sea surface approximately 9
141 km long and 4 km wide adjacent to the Atlantis II transform valley (Fig. 1a) and ~19 km south of the
142 SWIR axis. An estimated 1.5–2.0 km of crust has been unroofed from the footwall during the uplift of
143 the core complex (Buck et al., 2005; Dick et al., 2000; Dick et al., 1999b; John et al., 2004) on the
144 detachment fault (Fig. 1b). The top layers of a typical oceanic crust sequence, that is the pillow
145 basalts and sheeted dykes, are missing from the top of the core, exposing massive gabbro at the
146 seafloor. Three holes have been drilled and core retrieved in the Atlantis Bank oceanic core complex
147 (MacLeod et al., 2017). Here we investigate a sample from the first of these cores, 735B
148 (32°43.392'S, 57°15.960'E) initially drilled to 500 mbsf on IODP expedition 118, then extended to
149 1508 mbsf on IODP expedition 176 (Dick et al., 1999a).

150 The following core summary is based on information in Dick et al. (1999b), unless otherwise
151 specified. The core has been divided into 12 rock units (I to XII) based primarily on mineral
152 assemblage and abundance of the rock types. The rock units are variably metamorphosed at low
153 pressure and variable temperatures and are overprinted at the top of the core by brittle failure as
154 the rocks cooled and hydrothermal alteration accompanied deformation. The major rock types in
155 the core are olivine gabbro (69.9%) and gabbro (14.9%), with lower proportions of oxide-rich gabbro
156 (7%) and gabbronorite/oxide-rich gabbronorite (8%). The two predominant rock groups based on
157 iron and titanium oxide content (Dick et al., 2002; Hertogen et al., 2002) are (1) oxide-poor gabbro
158 cut by hundreds of bodies of (2) oxide gabbro, rich in ilmenite and magnetite; these oxide-rich
159 gabbros are also commonly rich in enstatite and brown hornblende. The oxide gabbro bodies vary
160 from undeformed patches in olivine gabbro to being spatially associated with high strain zones. Their
161 contacts with the oxide-poor gabbro bodies range from gradational to sharp (Dick et al., 2000).

162 Oxide abundance, occurrences of medium temperature veins (e.g. plagioclase, green hornblende
163 and/or diopside veins) and proportions of alteration products all decrease with depth and are
164 strongly correlated with an increase in crystal-plastic deformation intensity. The majority of the core
165 has no (75%) or very weak (18%) foliation due either to magmatic reorientation of crystals or crystal-
166 plastic deformation, with 6% being strongly foliated and only 1% showing mylonitic or ultra-
167 mylonitic characteristics. Major brittle faults of unknown displacement occur at 560 and 690–700
168 mbsf with many additional minor faults, displaying minor displacement, concentrated in the upper
169 50% of the core. A 20m wide shear zone occurs at 944–964 mbsf (Fig. 1c–g, Supplementary Fig. 1)
170 with many small shear zones of millimetre to centimetre widths occurring in the top of the core.
171 High strain zones are often associated with high oxide abundance. The sample analysed in this
172 contribution is taken from the middle of this 20m wide shear zone at 953.7 mbsf.

173 In addition to the comprehensive analysis of the core and its implications by the shipboard scientific
174 parties (Dick et al., 1999b), further analysis of the core has determined that crustal accretion of the
175 gabbros occurred for less than 0.5Myr around 12 Ma (Baines et al., 2009), that plagiogranites may
176 form by highly fractionated mid-ocean ridge basalts (Chen et al., 2019) or in-situ partial melting of
177 gabbro (e.g. Koepke et al., 2004; Wolff et al., 2013), and that synkinematic differentiation (Bowen,
178 1920) is an important magma evolution process in oceanic crust (Gao et al., 2007).

179 **3. Methods**

180 *3.1. Sample selection and general microscopic analyses*

181 The sample analysed was selected as it is representative of the broad tens of metre scale shear
182 zones commonly observed in the deformed gabbroic rocks (Fig. 1, Supplementary Fig. 1). It is from
183 953.7 mbsf in the 735B core, part of a 20m thick shear zone (Fig. 1c–g, Supplementary Fig. 1, 944 to
184 964 mbsf) at the base of rock unit X (the full rock unit X extent is from 710 – 964 mbsf). In addition, it
185 includes a narrow, well defined shear zone, a feature seen frequently in broad shear zones. The two

186 foliations associated with the broad and narrow shear zone, S_1 and S_2 respectively, are at an angle to
187 each other, however the azimuth of the lineations associated with these foliations are within a few
188 degrees of each other. The thin section studied was cut parallel to the lineation and perpendicular to
189 the foliation and was examined using plain and cross polarised light with a petrographic microscope.
190 A high-resolution image of the thin section and associated other data can be examined at
191 <https://imagematrix.science.mq.edu.au/viewer/?mode=view&id=19>). Backscattered electron (BSE)
192 images were taken of typical microstructures using a TESCAN VEGA3 scanning electron microscope
193 (SEM) at the Leeds Electron Microscopy and Spectroscopy Centre, University of Leeds. The SEM was
194 run at high vacuum with an accelerating voltage of 20 kV and working distance of 14.5 mm.

195 *3.2. Quantitative microstructural analysis*

196 Quantitative microstructural analysis was performed utilising Electron Backscatter Diffraction
197 analysis (EBSD). The thin section was polished using colloidal silica and coated with ~3 nm of carbon.
198 Crystallographic preferred orientation (CPO) information was collected using an HKL NordlysNano
199 detector attached to a Zeiss IVO SEM at the Macquarie GeoAnalytical laboratories, Macquarie
200 University. The SEM was run at a high vacuum with an accelerating voltage of 20 kV, a working
201 distance of 12.5 to 17 mm and a beam current of 8.0 nA. Points were analysed on a regular grid with
202 step sizes at 4 μm . The Kikuchi patterns acquired were automatically indexed using the Aztec
203 analysis software (Oxford Instruments). Concurrently, chemical maps were taken using an X-Max
204 energy dispersive spectrometry (EDS) detector allowing an independent control on mineral type and
205 abundance. Higher resolution maps were acquired using the Oxford Instruments Synergy EDS/EBSD
206 attached to a Zeiss Ultra Plus SEM at the Australian Centre for Microscopy and Microanalysis
207 (ACMM), University of Sydney. Here, accelerating voltage was 20 kV, working distance 8.55–10 mm
208 and step size 2 μm .

209 Data was processed using HKL Channel5 v5.11, with noise reduction performed on the raw data
210 following the procedure of Bestmann and Prior (2003). Phase maps of a representative subset of the

211 complete map acquired are shown (cf. Figs. 4, 5 and 7; images of the full EBSD data set are overlain
212 onto the high-resolution thin section images and are available at
213 <https://imagematrix.science.mq.edu.au/>), along with equal area, lower hemisphere pole figures of
214 the main minerals, constructed using data from the complete map based on one point per grain in
215 grey scale. Representations using one point per grain eliminate the issue of large grains distorting
216 the interpretation by causing single crystal maxima in the pole figures. For comparison, the relative
217 crystal orientation change of the large, relict grains is provided as a graded colour scale overlay on
218 the phase maps and pole figures. Misorientation angles between adjacent analysed points of 2–10°
219 and ≥ 10° define subgrain and grain boundaries, respectively.

220 *3.3. Major element mineral chemistry*

221 Major element mineral chemistry data were acquired on a Cameca SX100 electron microprobe
222 (EMP) equipped with 5 tuneable wavelength dispersive spectrometers at the Electron Microscopy
223 and X-ray Microanalysis Facility at The University of Tasmania. A spot size of 10 µm was used except
224 where the grain sizes were very small when a spot size of 5 µm was used. Operating conditions were
225 40° takeoff angle and a beam energy of 15 keV, counting for 10 to 30 seconds depending on the
226 element (see Supp. Table 1 for more details including standards used for calibration of the system).
227 Mineral formula from the EMP analyses were recalculated using 4 oxygen for olivine (Ol), 6 oxygen
228 for pyroxenes (Di and En) and ilmenite (Ilm), 8 oxygen for plagioclase (Pl) and 24 oxygen for
229 hornblende (Hbl). All hornblende mineral analyses are of brown hornblende. Representative mineral
230 analyses are included in Table 1 with the full dataset in Supp. Table 2. Variation in X_{Mg} is highlighted
231 for the minerals olivine, diopside, enstatite and hornblende using the mineral formula cation
232 calculations, where

$$X_{Mg} = \frac{(Mg)}{(Mg + Fe)}$$

233 Thin section element data was collected on the X-Ray Fluorescence Microscopy beamline, using the
234 Maia-384 detector on the Kirkpatrick-Baez mirror microprobe at the Australian Synchrotron,
235 Melbourne (Ryan et al., 2010a; Ryan et al., 2010b). Maps were made by collecting data with a step
236 size of 4µm x 4µm, beam energy of 18.5 keV, speed of 4 mm/sec and dwell time of 1 ms/step. A
237 calcium map was constructed using GeoPIXE (Ryan et al., 1990) to highlight the relative variation of
238 X_{An} in plagioclase across the thin section. X_{An} in plagioclase is calculated using the mineral formula
239 cation calculations from EMP data, where

$$X_{An} = \frac{(Ca)}{(Ca + Na)}$$

240 We use mineral abbreviations following Whitney and Evans (2010).

241 *3.4. Mineral thermometry*

242 Temperatures have been estimated using Putirka (2016) where hornblende compositions are
243 interrogated in conjunction with a liquid composition. For the latter, we used the composition of
244 MORB taken from samples near our core on the SWIR (Gale et al., 2013, sample SWIR48c). We also
245 present the Ridolfi and Renzulli (2012) hornblende thermometry calculations. We use Brey and
246 Köhler (1990) calcium in enstatite and two pyroxene thermometry calculations for comparison with
247 the hornblende thermometers. For thermometry calculations we assume pressures of 1 kbar. It
248 should be noted that the temperatures calculated have limited pressure sensitivity.

249 **4. Results**

250 *4.1. General sample description*

251 The olivine gabbro comprises olivine, diopside, and plagioclase, with minor enstatite, brown
252 hornblende, opaques (determined to be magnetite, ilmenite and sulphides) and apatite. The
253 analysed sample may be divided into two main domains based on differently oriented foliations (Fig.

254 2, 3). Domain I is characterised by the presence of coarse grains of olivine, diopside, plagioclase and
255 some enstatite. Here, a foliation (termed S_1) is defined by the alignment of elongate, coarse olivine,
256 plagioclase, diopside and enstatite porphyroclasts and associated, finer grained tails that occur
257 asymmetrically around the porphyroclasts and on the short side of the porphyroclasts (Fig. 2a, b, c,
258 4). In addition, brown hornblende is observed to occur as rims around diopside and olivine (Fig. 2a,
259 c, 5). Furthermore, symplectitic intergrowth of magnetite and enstatite are seen at the rims of
260 olivine grains (Fig. 6a-c). These latter reaction features are aligned with the Domain I foliation (Fig.
261 2). They are, however, distinct due to their link to reactions (see Sections 4.2 and 4.3). Hence, we
262 term the foliation which is microstructurally not associated with any changes to the mineral
263 assemblage S_{1a} and that associated with changes to the mineral assemblage S_{1b} . S_{1a} and S_{1b} are
264 subparallel to each other and are inferred to be progressive. Domain I dominates the whole 20m
265 thick shear zone (Fig. 1b, 2a, b, Supplementary Figure 1) from which the sample is taken. Domain II is
266 represented by a closely spaced foliation (termed S_2) oriented oblique to the pervasive S_1 foliation of
267 Domain I (Fig. 2a, b). Domain II has no olivine and is finer grained compared to Domain I; the large
268 porphyroclasts seen in Domain I are missing (Fig. 2, 3). There are areas where Domain I foliation
269 swings into the Domain II foliation suggesting that Domain II represents a narrow shear zone
270 displacing the pre-existing Domain I foliation. Both S_1 and S_2 are crosscut by a late narrow green
271 hornblende bearing vein (Fig. 2a, c). Areas near the hornblende vein have been avoided in this
272 analysis which is focused on the ductile tectono-metamorphic events.

273 *4.2. Domain 1: Mineral assemblages, microstructures and mineral chemistry*

274 *4.2.1. Igneous assemblage*

275 The average primary mode of olivine gabbro for the core, based on 118 samples from leg 176 is
276 plagioclase ~59.5%, diopside 29.9%, olivine 9.8%, opaques 0.4%, hornblende 0.3% and enstatite
277 0.2% (Dick et al., 1999a). In the analysed sample, the main original igneous minerals are plagioclase,
278 diopside and olivine with modal proportions within a few percent of the typical core average for this

279 rock unit; these grains are interpreted as igneous and original as they occur as large relict grains (Fig.
280 2a). The Ca element map (Fig. 3a) which correlates with the crossed polar (XPL) thin section image
281 (Fig. 3b) shows that the original relict plagioclase (Fig. 3a, b, centre top; marked PI (lg)) has a very
282 high Ca content signifying a high X_{An} value. Chemical microprobe analyses (Fig. 3a & c, Table 1, Supp.
283 Table 2) indicate the relict grains are labradorite in composition.

284 4.2.2. *Isochemical S_{1a} recrystallisation and foliation formation*

285 The alignment of the large elongate relict igneous grains (to ~3 mm) of olivine, diopside and
286 plagioclase (>200 μm diameter) define the distinct S_1 foliation (Fig. 2a). In addition, these phases are
287 also seen as fine-grained elongate masses, with variable grain sizes (averages of ~35 μm , Fig. 2a).
288 These masses commonly form tails developed adjacent to relict porphyroclasts of the same mineral
289 (Fig. 2a, d, 3b, 4a, b). Porphyroclasts exhibit abundant subgrain boundaries and continuous lattice
290 bending (gradual orientation change shown as slight colour change; e.g. Fig. 4c). This gradual to
291 sharp change in crystallographic orientation is also observed in pole figures (Fig. 4). In addition, some
292 medium to large plagioclase grains exhibit deformation twins (Fig. 3b inset). The smaller grains show
293 little internal orientation changes. It should be noted that next to a porphyroclast, the finer grains
294 tend to have a similar orientation to the porphyroclast. Small grains exhibit straighter grain
295 boundaries than porphyroclasts. Aspect ratios of large plagioclase and diopside grains are higher at
296 2.13 and 2.15, respectively, than the smaller grains at 1.83 and 1.81, respectively. Aspect ratios for
297 large and small olivine are similar at 1.73 (> 200 μm diameter) and 1.82 (<200 μm diameter)
298 respectively.

299 The Ca element map (Fig. 3a) shows that the original relict plagioclase has an associated
300 recrystallised tail of plagioclase which has a similar Ca value (i.e. labradorite, lightest orange),
301 indicating that no change of plagioclase composition occurred during formation of this recrystallised
302 tail.

303 Microprobe chemical analysis of the large and small olivine and diopside grains (Fig. 3d) shows little
304 to no variation indicating that no systematic change in the composition of these minerals occurred
305 during recrystallisation of the porphyroclast. Hence this foliation, defined by grain elongation and
306 recrystallisation into fine grained tails, is an exclusively geometric rather than chemical feature. We
307 refer to this foliation as S_{1a} .

308 *4.2.3. S_{1b} – foliation formation associated with melt presence: mineral assemblage and chemical*
309 *changes*

310 S_{1b} is identified through the presence of “new” minerals, namely enstatite on olivine (Fig. 5a) and
311 hornblende on diopside (Fig. 2d, 5b). These phases occur asymmetrically on the phase boundary
312 with plagioclase (e.g. Fig. 4a); they are concentrated in strain shadows on the larger olivine and
313 diopside grains (e.g. Fig. 4b), are smaller in grain size than the adjacent olivine and diopside and
314 exhibit variable grain sizes up to 200 μm .

315 S_{1b} microstructures show enstatite and hornblende grains form low dihedral angles and thin films
316 along grain boundaries (Fig. 6 a–c, black and red arrows, respectively). Enstatite shows embayments
317 into olivine (Fig. 6 a–c white arrows) and symplectites of magnetite and enstatite (Fig. 6a, green
318 arrow) are associated with olivine. Magnetite near enstatite and hornblende displays low dihedral
319 angles, forms thin films along grain boundaries (Fig. 6b) and can also have ilmenite exsolution
320 lamellae (Fig. 6d).

321 In S_{1b} , the chemistry of both hornblende and enstatite is distinct, depending on proximity to either
322 olivine or diopside. Enstatite grains associated with olivine (Fig. 3d green triangles) have a higher X_{Mg}
323 value than those grains associated with diopside (Fig. 3d orange triangles). In the same manner,
324 hornblende grains associated with olivine (Fig. 3d green circles) have a higher X_{Mg} value than those
325 grains associated with diopside (Fig. 3d orange circles).

326 The Synchrotron Ca–X_{An} map (Fig. 3a) shows that the chemistry of the finer grained plagioclase in
327 Domain I outside the original igneous grains and recrystallised tails, has lower calcium content and is
328 intermediate between labradorite and andesine (Fig. 3c) in composition. The histogram of electron
329 microprobe X_{An} calculations for all analysed plagioclase grains indicates a peak with X_{An} ~0.5. This
330 correlates with the larger area of S_{1b} reaction affected plagioclase as seen in the Synchrotron Ca–X_{An}
331 map (Fig. 3a).

332 Analysis of the CPOs of enstatite and hornblende associated with olivine (Fig. 5a) shows the strong
333 preferred orientation of olivine grains is reflected in the enstatite and to a lesser extent, hornblende.
334 That is, both enstatite and hornblende display a degree of epitaxy of the precursor olivine. Some of
335 the larger enstatite grains have minor internal deformation features i.e. little lattice bending and few
336 subgrain boundaries (Fig. 5a, 2° misorientation boundaries). Similarly, CPOs of hornblende and
337 enstatite associated with diopside (Fig. 5b) reflect the strong preferred orientation of the diopside
338 grains. Hence, both display epitaxy of the precursor diopside. However, very few of these reaction
339 products show any internal deformation (Fig. 5, misorientation profiles).

340 *4.3. Domain II: Mineral assemblages, microstructures and mineral chemistry*

341 The grains in Domain II are typically fine-grained forming strings of enstatite, diopside and/or
342 hornblende with minor apatite grains within fine grained plagioclase (Fig. 3b, 7a). These mostly
343 monomineralic strings define the closely spaced and distinct S₂ foliation (Figs. 2, 3a and b, 7a). No
344 olivine is present in Domain II and magnetite, ilmenite and other opaque minerals occur interstitially
345 (Fig. 6e), predominantly associated with hornblende and diopside. Diopside and plagioclase both
346 have average grain sizes of ~34 µm with very few grains greater than 200 µm. Enstatite and
347 hornblende are smaller, ~23 µm and ~14 µm, respectively, with no grains greater than 200 µm.
348 Just as in S_{1b}, there are intergrowths of magnetite and ilmenite (Fig. 6d green arrow) with low
349 dihedral angles, but here these are associated almost entirely with hornblende. In places,
350 hornblende forms faceted interstitial grains in contact with plagioclase (Fig. 6d). Ilmenite forms

351 crystallographically continuous, xenomorphic grains (Fig. 6e, f) occurring interstitially between
352 hornblende and magnetite grains. Due to the small grain size, few embayments and films can be
353 seen, but low dihedral angles are formed by all minerals. Small grains show little to no internal
354 lattice bending and/or subgrains. Only plagioclase, displaying some deformation twins and larger
355 enstatite grains have minor internal deformation with 2° misorientation boundaries (Fig. 7a). Pole
356 figures for the minerals indicate there is little to no CPO present (Fig. 7b). Whether the grains are
357 original S_1 grains recrystallised or newly formed in S_2 from further melt-rock reactions is difficult to
358 determine from the petrography and EBSD analysis alone.

359 In Domain II, the chemistry (Table 1) of enstatite has a lower X_{Mg} value, distinct (Fig. 3d, red
360 triangles) from that of the S_{1b} enstatite indicating this is newly formed enstatite. Diopside too has a
361 distinct Domain II / S_2 chemistry with lower X_{Mg} values compared to S_1 (Fig. 3d, red diamonds)
362 indicating newly formed diopside in S_2 . The chemistry of hornblende overlaps with that of the S_{1b}
363 hornblende and has a proportion of grains with distinctly higher X_{Mg} values (Fig. 3d, red circles). The
364 Synchrotron Ca- X_{An} map shows the chemistry of plagioclase is also distinct in parts of the S_2 domain
365 (Fig. 3a, blue colours). Electron microprobe analysis shows that within Domain II the finest grained
366 plagioclase is more Na-rich andesine (Fig. 3c), while the larger grains are transitional labradorite to
367 andesine similar to the S_{1b} plagioclase grains (Fig. 3a-c).

368 *4.4. Thermometry: Conditions of formation and deformation*

369 In the following we present temperature calculations for the different stages of the development of
370 strain localisation observed in our samples. Calculations are based on the described microstructural
371 context and mineral chemistry (Table 1, Supp. Table 2) and are summarised in Figure 8 (note
372 reference provided relate to the thermometer used). Temperatures for S_{1b} hornblende, a reaction
373 product, determined using the method of Putirka (2016) range from 863–969°C with a median of
374 949°C. This overlaps the temperature range, using the same method, for the S_2 grains of 869–965°C
375 with a median of 905°C. The hottest temperature estimates in S_{1b} are hornblende analyses adjacent

376 to olivine. The Ridolfi and Renzulli (2012) hornblende thermometer gives slightly lower temperature
377 ranges: for S_{1b} the range is 846–961°C with a median of 906°C, and for S_2 it is 753–946°C with a
378 median of 840°C.

379 Calculated temperature estimates using Ca in enstatite (Brey and Köhler, 1990), also a reaction
380 product in this sample, are hotter than the hornblende temperature estimates, giving a range for S_1
381 of 907–1093°C with a median of 1026°C, and for S_2 of 929–1058°C with a median of 1000°C. Again,
382 the hottest temperatures in S_1 are enstatite analyses adjacent to olivine. Adjacent pairs of enstatite
383 and diopside in S_2 analysed using the two pyroxene thermometer of Brey and Köhler (1990) give a
384 range for S_2 of 798–823°C with a median of 817°C, which is much cooler than the alternative
385 thermometers. The high temperatures determined from the reaction products have a slightly lower
386 range in S_2 compared with S_{1b} . High temperatures can also be inferred from the presence of brown
387 hornblende in both S_{1b} and S_2 . Overall, a general minor trend to lower temperatures is apparent
388 from the igneous solidus temperature to the S_{1b} and S_2 melt-rock interaction temperatures.

389 It should be noted that interpretation of the thermometers is difficult due to the variation in
390 hornblende and enstatite chemistry associated with their igneous reactant minerals and the
391 possibility of minerals formed during S_{1b} being recrystallised in S_2 .

392 **5. Discussion**

393 *5.1. Progressing strain localisation: transition from solid-state to melt-* 394 *present deformation*

395 The crosscutting relationship between Domain I and Domain II (Fig. 2a) and the progressive
396 deflection of the foliation dominating Domain I into Domain II allows us to determine that S_1 related
397 to Domain I is an earlier fabric than S_2 that dominates Domain II. In the following, we describe the
398 fabrics and their relationship to the progression of strain localisation in chronological sequence.

399 5.1.1. *S_{1a} melt absent solid-state deformation*

400 Dick et al. (1999b) differentiate magmatic fabric from crystal-plastic deformation fabric based on
401 microstructures. Magmatic fabric has subhedral plagioclase with no recrystallisation and pyroxenes
402 with sharp “corners” (Fig. 9a). Their crystal-plastic solid-state deformation overprint (corresponding
403 to our *S_{1a}*) has recrystallised plagioclase and elongate pyroxenes with rounded “corners”. Even
404 though magmatic foliations occur in ~22% of the core, magmatic foliation with no crystal plastic
405 overprint is extremely rare (see Dick et al., 1999b, their Fig. F79). This indicates that deformation
406 localised at the tens of metre scale during the *S_{1a}* event.

407 In our sample, *S_{1a}* displays igneous porphyroclasts (Ol-Di-Pl) that have grain boundaries that are not
408 facets and dynamically recrystallised tails forming foliation parallel bands and strain shadows (Fig. 2,
409 3a, b, 9b). Dislocation creep dominates *S_{1a}* solid-state deformation based on the facts that the large
410 grains display undulose extinction and are internally deformed (Fig. 3b, 4), form elongated grains
411 (Fig. 2, 3b and 4), have a distinct CPO suggesting dislocation creep with dominance of certain slip
412 systems (Fig. 4) and show progressive rotation across the grains (e.g. Fig. 4c). Dynamic
413 recrystallisation resulted in the formation of smaller grains with little internal deformation and lower
414 aspect ratios, often occurring as tails on the larger porphyroclasts. As the minerals are recrystallised,
415 the grain size decreases and phases are mixed, local switches from dislocation creep to diffusion
416 creep accommodated grain boundary sliding, for the recrystallised minerals, result in rheological
417 weakening (Mehl and Hirth, 2008).

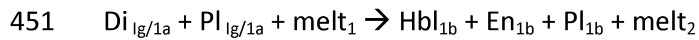
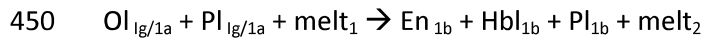
418 The igneous and *S_{1a}* mineral assemblages are identical and recrystallised grains are isochemical with
419 respect to their igneous precursors (Fig. 3a), suggesting *S_{1a}* deformation occurred in conditions close
420 to those prevalent during magmatic crystallisation in fluid/melt absent conditions. Hence, we infer
421 that deformation conditions were close to the low pressure solidus temperature of the olivine-
422 gabbro, which is estimated to be ~1080°C assuming tholeiitic MORB composition (Green, 1982).
423 Mehl and Hirth (2008) determined a cooler temperature range of ~860 to 940°C based on two
424 pyroxene thermometry.

425 5.1.2. *S_{1b} melt-present strain localisation: initial flux of an externally derived melt by porous melt*
426 *flow*

427 *S_{1b}* can be distinguished from *S_{1a}* by the additional presence of enstatite and brown hornblende,
428 observed in epitaxial reaction textures or rims on both olivine and diopside porphyroclasts (Fig. 5,
429 8c). Olivine predominantly forms enstatite with some hornblende (Fig. 5a) while diopside
430 predominantly forms hornblende with some enstatite (Fig. 2d, 5b).

431 Reaction textures are fine-grained, discontinuous and hydrous, including newly crystallised
432 plagioclase with or without diopside, and with minor ilmenite, magnetite, sulphides and apatite.
433 Magnetite occurs as single grains and in symplectite textures with enstatite (Fig. 6a), which suggest
434 diffusion-limited reactions of the melt with olivine (Holness et al., 2011). Microstructures indicative
435 of the former presence of melt (Lee et al., 2018; Stuart et al., 2017) in the reaction textures,
436 including low dihedral angles, films along grain boundaries and embayments (Fig. 6a-c, 9c) confirm
437 melt is the reactive agent and the source of water to form hornblende. Enstatite and hornblende
438 reaction textures are most common in foliation parallel bands, strain shadows and at mineral phase
439 boundaries (Fig. 4a, b, 5). Some reactant grains (olivine and diopside) show discontinuous and
440 asymmetric development of reaction products, highlighting that reactions must have been triggered
441 by fluid presence rather than being diffusion driven (Stuart et al., 2016). Based on the associated
442 melt present microstructures, we suggest that these reaction textures mark melt pathways with
443 melt fluxing along one side of the grain on the boundary between different mineral types (Fig. 4a, b,
444 9c). The melt pathways may additionally be identified by foliation parallel bands of lower calcium
445 plagioclase (Fig. 3a). The modification of plagioclase mineral chemistry and hydration to form
446 hornblende both indicate an open system involving flux of an externally derived melt.

447 The microstructures indicative of the former presence of melt as well as the variations from *S_{1a}* to *S_{1b}*
448 chemistry suggest enstatite, hornblende and the chemically distinct plagioclase are all reaction
449 products of two melt-rock reactions:



452 Besides changes in the stable assemblage, the grain size of reaction products is greatly reduced
453 relative to the reactant grains. Reaction products have average grain sizes of $\sim 35\mu m$ (Fig. 4). Thus, in
454 areas dominated by reaction products diffusion creep/grain boundary sliding is expected to be active
455 locally (Etheridge and Wilkie, 1979). This stands in contrast to some of the larger enstatite grains
456 which have minor internal deformation features, i.e. little lattice bending and few subgrain
457 boundaries (Fig. 5a, 2° misorientation boundaries) indicating these grains are residual from the
458 earlier solid state crystal plastic deformation event associated with S_{1a} .

459 The described microstructures and melt-induced reactions require that melt migrates along grain
460 boundaries. We suggest that during solid state deformation and associated dynamic recrystallisation
461 associated with the formation of S_{1a} , areas dominated by fine grained recrystallised grain acted as
462 preferred melt pathways due to the local high grain boundary length versus area and potential
463 porosity generation during recrystallisation and incipient grain boundary migration (Fusseis et al.,
464 2009). Once the first melt reacts, grain sizes are further reduced, and activation of grain boundary
465 sliding then creates additional porosity (Menegon et al., 2015).

466 Thermometry using reaction products such as hornblende (Putirka, 2016; Ridolfi and Renzulli, 2012)
467 and Ca in enstatite (Brey and Köhler, 1990) return a broad range of temperatures between ~ 840 to
468 $1100^\circ C$ (Fig. 8) due to variation in the mineral chemistry (Table 1). The spatial context of the
469 hornblende thermometry controls some of this range with olivine reaction products returning higher
470 temperatures ($> 920^\circ C$) than diopside reaction products ($< 960^\circ C$). The highest temperatures ($>$
471 $970^\circ C$) are only derived from Ca in enstatite thermometry (Fig. 8). The broad temperature range can
472 be explained by a variation in the temperature recorded throughout a melt fluxing event. High
473 temperatures record the melt-rock interaction at relatively high melt flux rates when temperatures

474 are dominated by the temperature of the fluxing melt. High temperatures for deformation in S_{1b} are
475 also supported by little variation in the composition of the recrystallised olivine, diopside and
476 plagioclase from their igneous and S_{1a} counterparts. Maintenance of high temperatures throughout
477 melt rock reaction may have been aided by the exothermic reaction involved in the formation of
478 hornblende (Haack and Zimmermann, 1996). In contrast, low recorded temperatures are interpreted
479 to represent the timing of reactions when melt flux was waning and temperatures became therefore
480 dominated by the temperature of the surrounding “host” rock that was being fluxed by the melt. As
481 such the overall range of temperatures can be taken as a signature of decreasing temperature of the
482 host rock during progressive deformation and decreasing melt flux. The high local variation of
483 derived temperatures may reflect the effect of multiple episodes of melt flux of increased and
484 waning melt flux.

485 *5.1.3. S_2 melt-present strain localisation: subsequent syntectonic highly channelised flux of an*
486 *externally derived melt*

487 The S_2 foliation cuts S_1 at approximately 30° and causes deflection of the S_1 foliation in intermediate
488 strain domains indicating a normal sense of motion (Fig. 2a, b). It is defined by very fine-grained (up
489 to $34\ \mu\text{m}$) plagioclase-, enstatite-, hornblende- or diopside-rich bands or mixtures of these minerals
490 (Fig. 2d, 7, 9d). Microstructures indicative of the former presence of melt in S_2 include (1) low
491 dihedral angles and films along grain boundaries (plagioclase, enstatite, magnetite and ilmenite, Fig.
492 6d-f), (2) undeformed ilmenite displaying a neighbourhood of apparently isolated grains with similar
493 orientation, suggesting these are a single crystal connected in 3D that pseudomorphed the
494 interconnected melt in that area (Fig. 6f), and (3) intergrown enstatite and hornblende sharing some
495 straight grain boundaries consistent with low index crystal faces indicating growth in the presence of
496 melt (Fig. 6d; Stuart et al., 2018b).

497 Hornblende in S_2 has a range of compositions overlapping those of S_1 , suggesting some hornblende
498 is residual in Domain II. In contrast, the analysed diopside and enstatite in S_2 have distinct mineral

499 chemistry, with lower X_{Mg} values, compared with their igneous or S_{1a} precursors and the range of
500 compositions has narrowed (Fig. 3). Some enstatite is likely to be residual as some larger grains show
501 internal deformation (e.g. Fig 7a). Plagioclase has a more sodic composition in S_2 compared with the
502 igneous and S_1 precursors (Fig. 3a, c). These relationships suggest recrystallisation and growth at
503 different conditions both chemically and in terms of PT conditions than in Domain I. Furthermore,
504 just as for S_{1b} , within S_2 , apatite, ilmenite and magnetite are products of a reaction involving
505 hornblende and enstatite indicating enrichment of these minerals during melt-rock interaction in
506 accordance with the original ODP reports (Dick et al., 2002; Hertogen et al., 2002). S_2 envelops rare
507 small porphyroclasts of diopside and plagioclase and all olivine has reacted away. We infer that the
508 following unbalanced open system reaction forms minerals in the S_2 high strain zone:

509 <all previous minerals> + externally derived melt \rightarrow $En_2 + Hbl_2 + Pl_2 + Di_2 +$ modified melt

510 These very small grains show minor crystal plastic deformation within individual grains and a low
511 degree of CPO suggesting a change of dominant deformation mechanism from dislocation creep
512 towards a deformation mechanism largely independent of dislocation movement. Based on the
513 observed microstructures indicative of the former presence of melt, the apparent small grain size,
514 minor CPO and absence of orientation changes, we infer deformation within Domain II/ S_2 was
515 dominated by grain size dependent melt assisted grain boundary sliding and diffusion creep
516 (Etheridge and Wilkie, 1979; Stuart et al., 2018b; White, 1976). Furthermore, we propose that
517 syntectonic channelised porous melt flow occurred in this localised zone. We suggest the highly
518 localised nature of the porous melt is facilitated by grain boundary sliding of the fine-grained
519 reaction products which results in transient porosity and a “melt pump” (Fusseis et al., 2009;
520 Menegon et al., 2015). This positive feedback and switch in dominant deformation mechanism
521 resulted therefore, in significant rheological weakening (e.g. Smith et al., 2015) enhanced by the
522 presence of melt as melt presence along grain boundaries will make these melt zones extremely
523 weak (Rosenberg and Handy, 2005). The latter rheological weakening is enhanced by extensive grain

524 size reduction by syntectonic reaction forming fine grained enstatite and hornblende and resulting in
525 a marked increase in melt-bearing grain boundaries. This facilitates increased melt flux, further
526 enhancing reactions and grain size reduction, resulting in further weakening and strain localisation.
527 Local volume increase (e.g. from formation of hornblende) may also assist in enhancing melt flux
528 pathways facilitating increased melt flux (Rushmer, 2001).

529 Conditions for deformation from hornblende (Putirka, 2016; Ridolfi and Renzulli, 2012) and two
530 pyroxene (Brey and Köhler, 1990) thermometry suggest a range of temperatures between ~750 to
531 965°C (Fig. 8). The highest temperatures are similar for S_{1b} and S_2 , the lowest temperatures (< 825°C)
532 are lower in S_2 than for S_{1b} . The wide range of recorded temperatures can be explained similarly to
533 the S_{1b} temperature range. That is, high temperatures record the melt-rock interaction at high melt
534 flux rates while low recorded temperatures represent low melt flux recording the temperature of
535 the “host” rock. Consequently, the decrease of the lowest recorded temperatures from S_{1b} to S_2 is
536 consistent with gradual cooling of the system during development and exhumation of the core
537 complex. This interpretation of temperatures is consistent with the observed anomalously high
538 temperatures late in the detachment complex formation reported by John et al. (2004). Their Model
539 2 suggests this anomaly could be due to reheating by a late flux of melt, similar to the S_2 event
540 described here. Furthermore, Magde et al. (1995) reported hornblende veins in rock unit VI (400-500
541 mbsf) interpreted as a possible melt flux deformation event when the matrix was >500°C. As the
542 melt flux diminished, and finally stopped, the interstitial melt crystallised allowing the preservation
543 of the delicate microstructures indicative of the former presence of melt, and causing our sample to
544 become rheologically hard (Stuart et al., 2018b).

545 *5.2. Melt transport and origin of melt*

546 The mechanisms of melt transport in ocean core complexes has been an ongoing discussion.
547 Members of the ODP Leg 118 and 176 teams (Dick et al., 1991; Dick et al., 1999a; Niu et al., 2002)
548 interpret that deformation of a gabbro crystal mush drove local accumulation of intercumulus liquids

549 into shear zones to form the oxide gabbro bodies. Melt-present deformation of a gabbro crystal
550 mush is evidenced in some portions of the 735B core, by a magmatic foliation (e.g. Fig. 9a), defined
551 by a strong shape preferred orientation of the primary crystals (olivine, diopside, plagioclase) which
552 lack significant internal deformation. In these samples, plagioclase displays some deformation twins,
553 lobate grain boundaries and a strong CPO and olivine has minor dislocations. These observations
554 support the interpretation of viscous laminar flow of a crystal mush with a minor solid-state
555 deformation overprint (Cannat et al., 1991). However, this magmatic foliation is not seen in the
556 sample studied here.

557 In Section 5.1, we demonstrate that the strain localisation history in our sample started in the solid-
558 state as also observed by Mehl and Hirth (2008) and Miranda and John (2010). While the study of
559 Miranda and John (2010) focused on samples, acquired by submersible dives, that progressed to
560 hydrothermal fluid-present deformation, we show that in our core sample initial solid-state
561 deformation was followed by melt present deformation involving an externally-derived melt. This
562 interpretation is consistent with previous studies which suggest the presence of melt in the system:
563 (i) mantle-like $\delta^{18}\text{O}$ values for all olivine, diopside and plagioclase deeper than 800 mbsf, precluding
564 a hydrothermal source for the hornblende-producing reactions (Gao et al., 2006); (ii) rare earth
565 element (REE) patterns of hornblende are consistent with crystallisation from a melt (Gillis and
566 Meyer, 2001); (iii) a REE study on clinopyroxene from 880 mbsf by Gao et al. (2007) showed no
567 seawater signature; (iv) postulated late high temperature melt flux (John et al., 2004; Magde et al.,
568 1995).

569 A consequence of our interpretation is that melt fluxed the system and was transported within the
570 zones of strain localisation. This interpretation of the importance of high strain zones for the
571 transport of melt is supported by field studies (Schulmann et al., 2008), analogue experiments
572 (Holtzman et al., 2003; Qi et al., 2018; Qi et al., 2015; Walte et al., 2003) and numerical models

573 (Llorens et al., 2019) that show melt accumulates into shear bands during deformation of a mixed
574 rheology material.

575 In our view, a cumulus melt source for the external melt is likely and melt rock reaction enriched the
576 deforming rock in enstatite, hornblende, ilmenite, magnetite and apatite. Dick et al. (1991) make a
577 genetic link between the host gabbro and the oxide gabbro bodies. While their interpretation
578 focuses on melt migration and accumulation at the pluton scale, they also allow for some melt
579 escape into solid overlying gabbro country rock along shear zones, and suggest prolonged melt flux
580 and impregnation of Fe-Ti oxides precipitated from the migrating melt may have formed rocks with
581 up to 50% oxides; i.e. these rocks formed by prolonged reactive melt flow. This contrasts with the
582 interpretation of Cannat (1991) who suggested that mylonite zones preferentially localised in
583 primary oxide-rich layers. We suggest the Fe-Ti oxides are crystallised late in the melt flux,
584 pseudomorphing the melt locations and subsequently display little to no internal deformation as
585 shown by the low internal deformation exhibited by interstitial ilmenite grains that are connected in
586 3D in our samples (Fig. 6e, f). An alternate source of melt in MOR settings is partial melting of gabbro
587 under hydrous conditions (e.g. Wolff et al., 2013). However, this produces felsic rock types and the
588 mantle like $\delta^{18}\text{O}$ values from core deeper than 800 mbsf (Gao et al., 2006) precludes this as the melt
589 source for our sample.

590 *5.3. The importance of melt present deformation in strain localisation in the* 591 *oceanic crust*

592 Our analysis shows a progressive increase in strain localisation where melt presence plays a
593 significant role (Fig. 9). To evaluate the importance of melt present deformation it is important to
594 identify the key features used to distinguish solid state deformation in melt-absent conditions from
595 melt present deformation scenarios. The key features used to identify solid-state deformation in
596 melt-absent conditions are a lack of (1) assemblage changes and reaction textures, (2) chemical
597 changes from remnant to recrystallized grains, (3) microstructures indicative of the former presence

598 of melt (Fig. 9). These features are all absent in our sample during development of S_{1a} , whereas the
599 opposite is true for the development of S_{1b} and S_2 where we infer melt to have been present during
600 the deformation.

601 Based on our analysis we propose the following evolution of the oceanic gabbroic crust. First, upon
602 magma cooling the melt crystallises between the liquidus of $\sim 1210^\circ\text{C}$ (Green, 1982), where the first
603 minerals are crystallised, to subsolidus temperatures of $\sim 1080^\circ\text{C}$ (Green, 1982), where the gabbro is
604 fully crystalline. Dependent upon magmatic conditions, some gabbro forms a magmatic foliation
605 (Fig. 9a), while most forms a less foliated igneous texture (Fig. 1f, g(i)). As stress is applied to the rock
606 mass, deformation is initially accommodated at the tens of metre scale (Gardner et al., 2019), by
607 solid state deformation; i.e., dislocation creep processes (Fliervoet et al., 1999; Urai et al., 1986),
608 causing lattice distortions, subgrain formation and dynamic recrystallisation resulting in grain size
609 reduction and some rheological weakening (Figs. 4, 9b).

610 This deformation also creates locally a high number of grain boundaries and pores forming pathways
611 for subsequent open system diffuse porous melt flow (Daczko et al., 2016; Meek et al., 2019; Stuart
612 et al., 2018a; Stuart et al., 2018b); the melt possibly being derived from an inter-cumulus melt lower
613 in the crust (Dick et al., 1991). As externally-derived melt migrates along grain boundaries and
614 between smaller grains during deformation, melt-rock reactions introduce new minerals (enstatite
615 and hornblende) with further reduced grain sizes (e.g. Stuart et al., 2016; White and Knipe, 1978). As
616 the mineral grain sizes decrease the deformation evolves to melt present deformation involving both
617 dislocation creep and melt assisted grain boundary sliding in the fine-grained areas. This causes
618 strain localisation in areas of melt flux and melt rock interactions (Fig. 9c; Lee et al., 2018; Meek et
619 al., 2019; Stuart et al., 2018a) . During a second episode of deformation and melt flux an effective
620 positive feedback loop is created, where local melt assisted grain boundary sliding within areas of
621 fine grained reaction products result in an active porosity pumping system (Fusseis et al., 2009;
622 Menegon et al., 2015). This in turn, facilitates increased melt flux through the system channelizing
623 melt in one area (Fig. 9d). In this local zone, further melt rock reaction and associated grain size

624 reduction results in enhanced melt flux. Consequently, in this narrow zone extreme rheological
625 weakening occurs as all grain boundaries are becoming melt filled and the rheology is dominated by
626 the rheology of the melt phase (Rosenberg and Handy, 2005). Consequently, strain is increasingly
627 localized into well-defined, narrow shear zones which exhibit near complete replacement of the
628 original mineralogy with the products of the melt rock reactions (Fig. 7, 9d).

629 **6. Conclusions**

630 Our study shows increasing strain localisation associated with solid-state deformation and
631 subsequent melt present deformation with migration of at least two externally derived highly
632 fractionated gabbroic melts, likely sourced from inter-cumulus melt extracted from deeper levels of
633 the oceanic lithosphere.

634 Microstructural analysis shows that strain becomes increasingly focused by: (1) dynamic
635 recrystallisation during melt-absent solid-state deformation dominated by dislocation creep (Fig 9b);
636 (2) diffusive melt-present deformation associated with a flux of an externally derived melt causing
637 melt-rock interactions and forming fine grained reaction products which in turn causes additional
638 weakening via melt assisted grain boundary sliding (Fig. 9c); (3) highly channelised flux of an
639 externally derived melt causing further reaction induced grain size reduction coupled with melt
640 assisted grain boundary sliding (Fig. 9d), which thereby creates a pumping system allowing large
641 volumes of melt to migrate and strain to localise in a narrow millimetre-scale zone.

642 In conclusion, our study demonstrates that syntectonic porous melt flow plays a major role in the
643 evolution of the oceanic crust, in particular in oceanic core complexes.

644 **Acknowledgements**

645 Logistical and analytical funding was provided by the Australian IODP Office (ANZIC Legacy Analytical
646 funding) and the Department of Earth and Environmental Sciences, Macquarie University. Part of
647 this research was undertaken on the X-Ray Fluorescence Microscopy beamline at the Australian
648 Synchrotron, Victoria, Australia (project 14351). This work was supported by the Multi-modal
649 Australian ScienceS Imaging and Visualisation Environment (MASSIVE, www.massive.org.au). The
650 authors would like to thank Karsten Gorman of University of Tasmania for his assistance collecting
651 the EMP data. We would also like to thank Nick Hayman and an anonymous reviewer for their
652 careful and constructive reviews, and Greg Shellnutt for editorial handling. This is contribution xxx
653 from the ARC Centre of Excellence for Core to Crust Fluid Systems (<http://www.cafs.mq.edu.au>) and
654 xxx in the GEMOC Key Centre (<http://www.gemoc.mq.edu.au>).

655 **References:**

656 Baines, A.G., Cheadle, M.J., John, B.E., Grimes, C.B., Schwartz, J.J., Wooden, J.L., 2009. SHRIMP Pb/U
657 zircon ages constrain gabbroic crustal accretion at Atlantis Bank on the ultraslow-spreading
658 Southwest Indian Ridge. *Earth and Planetary Science Letters* 287, 540-550.

659 Bestmann, M., Prior, D.J., 2003. Intragranular dynamic recrystallization in naturally deformed calcite
660 marble: diffusion accommodated grain boundary sliding as a result of subgrain rotation
661 recrystallization. *Journal of Structural Geology* 25, 1597-1613.

662 Bloomer, S.H., Meyer, P.S., Dick, H.J.B., Ozawa, K., Natland, J.H., 1991. 2. Textural and mineralogic
663 variations in gabbroic rocks from hole 735B, in: Von Herzon, R.P., Fox, J., Palmer-Julson, A.,
664 Robinson, P.T. (Eds.), *Proceedings of the International Ocean Drilling Program volume 118*.
665 International Drilling Program, Texas, pp. 21-39.

666 Bowen, N., L., 1920. Differentiation by deformation. *Proceedings of the National Academy of*
667 *Sciences* 6, 159-162.

668 Brey, G.P., Köhler, T., 1990. Geothermobarometry in Four-phase Lherzolites II. New
669 Thermobarometers, and Practical Assessment of Existing Thermobarometers. *Journal of Petrology*
670 31, 1353-1378.

671 Brodie, K.H., Rutter, E.H., 1987. The role of transiently fine-grained reaction products in syntectonic
672 metamorphism: natural and experimental examples. *Canadian Journal of Earth Sciences* 24, 556-564.

673 Buck, W.R., Lavier, L.L., Poliakov, A.N.B., 2005. Modes of faulting at mid-ocean ridges. *Nature* 434,
674 719-723.

675 Bürgmann, R., Dresen, G., 2008. Rheology of the Lower Crust and Upper Mantle: Evidence from Rock
676 Mechanics, Geodesy, and Field Observations. *Annual Review of Earth and Planetary Sciences* 36,
677 531-567.

678 Cannat, M., 1991. 22. Plastic deformation at an oceanic spreading ridge: a microstructural study of
679 the site 735 gabbros (Southwest Indian Ocean), in: Von Herzon, R.P., Fox, J., Palmer-Julson, A.,
680 Robinson, P.T. (Eds.), *Proceedings of the International Ocean Drilling Program volume 118. Ocean*
681 *Drilling Program, Texas*, pp. 399-408.

682 Cannat, M., Mével, C., Stakes, D., 1991. 24. Normal ductile shear zones at an oceanic spreading
683 ridge: tectonic evolution of site 735 gabbros (Southwest Indian Ocean), in: Von Herzon, R.P., Fox, J.,
684 Palmer-Julson, A., Robinson, P.T. (Eds.), *Proceedings fo the Ocean Drilling Program, scientific results*
685 *volume 118. Ocean Drilling Program, Texas*, pp. 415-429.

686 Chen, Y., Niu, Y., Wang, X., Gong, H., Guo, P., Gao, Y., Shen, F., 2019. Petrogenesis of ODP Hole 735B
687 (Leg 176) Oceanic Plagiogranite: Partial Melting of Gabbros or Advanced Extent of Fractional
688 Crystallization? *Geochemistry, Geophysics, Geosystems* 0.

689 Cyprych, D., Piazzolo, S., Wilson, C.J.L., Luzin, V., Prior, D.J., 2016. Rheology, microstructure and
690 crystallographic preferred orientation of matrix containing a dispersed second phase: Insight from
691 experimentally deformed ice. *Earth and Planetary Science Letters* 449, 272-281.

692 Daczko, N.R., Piazzolo, S., Meek, U., Stuart, C.A., Elliott, V., 2016. Hornblendite delineates zones of
693 mass transfer through the lower crust. *Scientific Reports* 6, 31369.

694 Deans, J.R.L., Yoshinobu, A.S., 2019. Geographically re-oriented magmatic and metamorphic
695 foliations from ODP Hole 735B Atlantis Bank, Southwest Indian Ridge: Magmatic intrusion and
696 crystal-plastic overprint in the footwall of an oceanic core complex. *Journal of Structural Geology*
697 126, 1-10.

698 Dick, H.J.B., Meyer, P.S., Bloomer, S.H., Kirby, S.H., Stakes, D., Mawer, C., 1991. 26. Lithostratigraphic
699 evolution of an in-situ section of oceanic layer 3, in: Von Herzon, R.P., Fox, J., Palmer-Julson, A.,
700 Robinson, P.T. (Eds.), *Proceeding of the Ocean Drilling Program, Scientific Results Volume 118.*
701 *Ocean Drilling Program, Texas*, pp. 439-538.

702 Dick, H.J.B., Natland, J.H., Alt, J.C., Bach, W., Bideau, D., Gee, J.S., Haggas, S., Hertogen, J.G.H., Hirth,
703 G., Holm, P.M., Ildefonse, B., Iturrino, G.J., John, B.E., Kelley, D.S., Kikawa, E., Kingdon, A., LeRoux,
704 P.J., Maeda, J., Meyer, P.S., Miller, D.J., Naslund, H.R., Niu, Y.-L., Robinson, P.T., Snow, J., Stephen,
705 R.A., Trimby, P.W., Worm, H.-U., Yoshinobu, A., 2000. A long in situ section of the lower ocean crust:
706 results of ODP Leg 176 drilling at the Southwest Indian Ridge. *Earth and Planetary Science Letters*
707 179, 31-51.

708 Dick, H.J.B., Natland, J.H., Miller, D.J., Alt, J.C., Bach, W., Bideau, D., Gee, J.S., Haggas, S., Hertogen,
709 J.G.H., Hirth, G., Holm, P.M., Ildefonse, B., Iturrino, G.J., John, B., Kelley, D.S., Kikawa, E., Kingdon, A.,
710 Le Roux, P., Maeda, J., Meyer, P.S., Naslund, H.R., Niu, Y., Robinson, P.T., Snow, J.E., Stephen, R.A.,
711 Trimby, P., Worm, H.-U., Yoshinobu, A., 1999a. 1. Leg 176 Summary, in: Marin, J.A., Scroggs, J.M.
712 (Eds.), *Proceedings of the International Ocean Drilling Program, initial reports volume 176.* *Ocean*
713 *Drilling Program, Texas*, p. 70.

714 Dick, H.J.B., Natland, J.H., Miller, D.J., Alt, J.C., Bach, W., Bideau, D., Gee, J.S., Haggas, S., Hertogen,
715 J.G.H., Hirth, G., Holm, P.M., Ildefonse, B., Iturrino, G.J., John, B., Kelley, D.S., Kikawa, E., Kingdon, A.,
716 Le Roux, P., Maeda, J., Meyer, P.S., Naslund, H.R., Niu, Y., Robinson, P.T., Snow, J.E., Stephen, R.A.,
717 Trimby, P., Worm, H.-U., Yoshinobu, A., 1999b. 3. Site 735, in: Marin, J.A., Scroggs, J.M. (Eds.),
718 *Proceedings of the Ocean Drilling Program, initial reports volume 176.* *Ocean Drilling Program,*
719 *Texas*, pp. 1-313.

720 Dick, H.J.B., Ozawa, K., Meyer, P.S., Niu, Y., Robinson, P.T., Constantin, M., Hebert, R., Maeda, J.,
721 Natland, J.H., Hirth, J.G., Mackie, S.M., 2002. 10. Primary silicate mineral chemistry of a 1.5-km
722 section of very slow spreading lower ocean crust: ODP hole 735B, Southwest Indian Ridge, in:
723 Natland, J.H., Dick, H.J.B., Miller, D.J., Von Herzon, R.P. (Eds.), Proceedings of the Ocean Drilling
724 Program, scientific results volume 176. Ocean Drilling Program, Texas, pp. 1-61.

725 Eisenlohr, B., Groves, D., Partington, G., 1989. Crustal-scale shear zones and their significance to
726 Archaean gold mineralization in Western Australia. *Mineralium Deposita* 24, 1-8.

727 Etheridge, M.A., Wilkie, J.C., 1979. Grainsize reduction, grain boundary sliding and the flow strength
728 of mylonites. *Tectonophysics* 58, 159-178.

729 Fliervoet, T.F., Drury, M.R., Chopra, P.N., 1999. Crystallographic preferred orientations and
730 misorientations in some olivine rocks deformed by diffusion or dislocation creep. *Tectonophysics*
731 303, 1-27.

732 Fusseis, F., Regenauer-Lieb, K., Liu, J., Hough, R.M., De Carlo, F., 2009. Creep cavitation can establish
733 a dynamic granular fluid pump in ductile shear zones. *Nature* 459, 974-977.

734 Gale, A., Dalton, C.A., Langmuir, C.H., Su, Y., Schilling, J.-G., 2013. The mean composition of ocean
735 ridge basalts. *Geochemistry, Geophysics, Geosystems* 14, 489-518.

736 Gao, Y., Hoefs, J., Hellebrand, E., von der Handt, A., Snow, J.E., 2007. Trace element zoning in
737 pyroxenes from ODP Hole 735B gabbros: diffusive exchange or synkinematic crystal fractionation?
738 *Contributions to Mineralogy and Petrology* 153, 429-442.

739 Gao, Y., Hoefs, J., Przybilla, R., Snow, J.E., 2006. A complete oxygen isotope profile through the lower
740 oceanic crust, ODP Hole 735B. *Chemical Geology* 233, 217-234.

741 Gardner, R., Piazzolo, S., Daczko, N.R., Evans, L., 2019. Ductile deformation without localization:
742 Insights from numerical modelling. *Geochemistry, Geophysics, Geosystems* n/a.

743 Gardner, R.L., Piazzolo, S., Daczko, N.R., 2015. Pinch and swell structures: evidence for strain
744 localisation by brittle–viscous behaviour in the middle crust. *Solid Earth* 6, 1045-1061.

745 Gillis, K.M., Meyer, P.S., 2001. Metasomatism of oceanic gabbros by late stage melts and
746 hydrothermal fluids: Evidence from the rare earth element composition of amphiboles.
747 *Geochemistry, Geophysics, Geosystems* 2.

748 Green, T.H., 1982. Anatexis of mafic crust and high pressure crystallization of andesite, in: Thorpe,
749 R.S. (Ed.), *Andesites: orogenic andesites and related rocks*. Wiley, Chichester, pp. 465-487.

750 Haack, U., Zimmermann, H., 1996. Retrograde mineral reactions: a heat source in the continental
751 crust? *Geologische Rundschau* 85, 130-137.

752 Hansen, L.N., Zimmerman, M.E., Kohlstedt, D.L., 2011. Grain boundary sliding in San Carlos olivine:
753 Flow law parameters and crystallographic-preferred orientation. *Journal of Geophysical Research:*
754 *Solid Earth* 116, B08201.

755 Hertogen, J.G.H., R., E., Robinson, P.T., Erzinger, J., 2002. 6. Lithology, mineralogy and geochemistry
756 of the lower ocean crust, ODP hole 735B, Southwest Indian Ridge, in: Natland, J.H., Dick, H.J.B.,
757 Miller, D.J., Von Herzen, R.P. (Eds.), *Proceedings of the International Ocean Drilling Program,*
758 *Scientific Results, Volume 176. Ocean Drilling Program, Texas*, pp. 1-82.

759 Hobbs, B., Regenauer-Lieb, K., Ord, A., 2008. Folding with thermal–mechanical feedback. *Journal of*
760 *Structural Geology* 30, 1572-1592.

761 Hobbs, B.E., Ord, A., Spalla, M.I., Gosso, G., Zucali, M., 2010. The interaction of deformation and
762 metamorphic reactions. *Geological Society, London, Special Publications* 332, 189-223.

763 Holness, M.B., Cesare, B., Sawyer, E.W., 2011. Melted rocks under the microscope: microstructures
764 and their interpretation. *Elements* 7, 247-252.

765 Holtzman, B., Kohlstedt, D.L., Zimmerman, M.E., Heidelbach, F., Hiraga, K., Hustoft, J., 2003. Melt
766 Segregation and Strain Partitioning: Implications for Seismic Anisotropy and Mantle Flow. *Science*
767 301, 1227-1230.

768 Howell, S.M., Olive, J.-A., Ito, G., Behn, M.D., Escartín, J., Kaus, B., 2019. Seafloor expression of
769 oceanic detachment faulting reflects gradients in mid-ocean ridge magma supply. *Earth and*
770 *Planetary Science Letters* 516, 176-189.

771 Ji, S., Wang, Z., Wirth, R., 2001. Bulk flow strength of forsterite–enstatite composites as a function of
772 forsterite content. *Tectonophysics* 341, 69-93.

773 John, B.E., Foster, D.A., Murphy, J.M., Cheadle, M.J., Baines, A.G., Fanning, C.M., Copeland, P., 2004.
774 Determining the cooling history of in situ lower oceanic crust—Atlantis Bank, SW Indian Ridge. *Earth
775 and Planetary Science Letters* 222, 145-160.

776 Karson, J.A., 1999. Geological investigation of a lineated massif at the Kane Transform Fault:
777 Implications for oceanic core complexes. *Philosophical Transactions of the Royal Society of London.
778 Series A: Mathematical, Physical and Engineering Sciences* 357, 713-740.

779 Koepke, J., Feig, S.T., Snow, J., Freise, M., 2004. Petrogenesis of oceanic plagiogranites by partial
780 melting of gabbros: an experimental study. *Contributions to Mineralogy & Petrology* 146, 414-432.

781 Lavier, L.L., Roger Buck, W., Poliakov, A.N.B., 1999. Self-consistent rolling-hinge model for the
782 evolution of large-offset low-angle normal faults. *Geology* 27, 1127-1130.

783 Lee, A.L., Torvela, T., Lloyd, G.E., Walker, A.M., 2018. Melt organisation and strain partitioning in the
784 lower crust. *Journal of Structural Geology* 113, 188-199.

785 Llorens, M.-G., Gomez-Rivas, E., Ganzhorn, A.-C., Griera, A., Steinbach, F., Roessiger, J., Labrousse, L.,
786 Walte, N.P., Weikusat, I., Bons, P.D., 2019. The effect of dynamic recrystallisation on the rheology
787 and microstructures of partially molten rocks. *Journal of Structural Geology* 118, 224-235.

788 MacLeod, C.J., Dick, H.J.B., Blum, P., Abe, N., Blackman, D.K., Bowles, J.A., Cheadle, M.J., Cho, K.,
789 Ciazeka, J., Deans, J.R., Edgcomb, V.P., Ferrando, C., France, L., Ghosh, N., Ildefonse, B., Kendrick,
790 M.A., Koepke, J.H., Leong, J.A.M., Liu, C., Ma, Q., Morishita, T., Morris, A., Natland, J.H., Nozaka, T.,
791 Pluemper, O., Sanfilippo, A., Sylvan, J.B., Tivey, M.A., Tribuzio, R., Viegas, L.G.F., 2017. Expedition 260
792 summary. *Proceedings of the International Ocean Discovery Program* 360, 27.

793 Magde, L.S., Dick, H.J.B., Hart, S.R., 1995. Tectonics, alteration and the fractal distribution of
794 hydrothermal veins in the lower ocean crust. *Earth and Planetary Science Letters* 129, 103-119.

795 Meek, U., Piazzolo, S., Daczko, N.R., 2019. The field and microstructural signatures of deformation-
796 assisted melt transfer: Insights from magmatic arc lower crust, New Zealand. *Journal of*
797 *Metamorphic Geology* 37, 795-821.

798 Mehl, L., Hirth, G., 2008. Plagioclase preferred orientation in layered mylonites: Evaluation of flow
799 laws for the lower crust. *Journal of Geophysical Research: Solid Earth* 113, n/a-n/a.

800 Menegon, L., Fousseis, F., Stünitz, H., Xiao, X., 2015. Creep cavitation bands control porosity and fluid
801 flow in lower crustal shear zones. *Geology* 43, 227-230.

802 Miranda, E.A., John, B.E., 2010. Strain localization along the Atlantis Bank oceanic detachment fault
803 system, Southwest Indian Ridge. *Geochemistry, Geophysics, Geosystems* 11.

804 Niu, Y., Gilmoie, T., Mackie, S.M., Greig, A., Bach, W., 2002. 8. Mineral chemistry, whole-rock
805 compositions, and petrogenesis of leg 176 gabbros: data and discussion, in: Natland, J.H., Dick,
806 H.J.B., Miller, D.J., Von Herzon, R.P. (Eds.), *Proceeding of the Ocean Drilling Program, scientific*
807 *results volume 176*. Ocean Drilling Program, Texas, pp. 1-60.

808 Olive, J.-A., Behn, M.D., Tucholke, B.E., 2010. The structure of oceanic core complexes controlled by
809 the depth distribution of magma emplacement. *Nature Geoscience* 3, 491-495.

810 Putirka, K., 2016. Amphibole thermometers and barometers for igneous systems and some
811 implications for eruption mechanisms of felsic magmas at arc volcanoes. *American mineralogist* 101,
812 841-858.

813 Qi, C., Hansen, L.N., Wallis, D., Holtzman, B.K., Kohlstedt, D.L., 2018. Crystallographic Preferred
814 Orientation of Olivine in Sheared Partially Molten Rocks: The Source of the “a-c Switch”.
815 *Geochemistry, Geophysics, Geosystems* 19, 316-336.

816 Qi, C., Kohlstedt, D.L., Katz, R.F., Takei, Y., 2015. Experimental test of the viscous anisotropy
817 hypothesis for partially molten rocks. *Proceedings of the National Academy of Sciences* 112, 12616-
818 12620.

819 Renner, J., Evans, B., Hirth, G., 2000. On the rheologically critical melt fraction. *Earth and Planetary*
820 *Science Letters* 181, 585-594.

821 Ridolfi, F., Renzulli, A., 2012. Calcic amphiboles in calc-alkaline and alkaline magmas:
822 thermobarometric and chemometric empirical equations valid up to 1,130°C and 2.2 GPa.
823 Contributions to Mineralogy and Petrology 163, 877-8995.

824 Rosenberg, C.L., Handy, M.R., 2005. Experimental deformation of partially melted granite revisited:
825 implications for the continental crust. Journal of Metamorphic Geology 23, 19-28.

826 Rushmer, T., 2001. Volume change during partial melting reactions: implications for melt extraction,
827 melt geochemistry and crustal rheology. Tectonophysics 342, 389-405.

828 Ryan, C.G., Cousens, D.R., Sie, S.H., Griffin, W.L., Suter, G.F., Clayton, E., 1990. Quantitative pixe
829 microanalysis of geological material using the CSIRO proton microprobe. Nuclear Instruments and
830 Methods in Physics Research Section B: Beam Interactions with Materials and Atoms 47, 55-71.

831 Ryan, C.G., Kirkham, R., Hough, R.M., Moorhead, G., Siddons, D.P., de Jonge, M.D., Paterson, D.J., De
832 Geronimo, G., Howard, D.L., Cleverley, J.S., 2010a. Elemental X-ray imaging using the Maia detector
833 array: The benefits and challenges of large solid-angle. Nuclear Instruments and Methods in Physics
834 Research Section A: Accelerators, Spectrometers, Detectors and Associated Equipment 619, 37-43.

835 Ryan, C.G., Siddons, D.P., Kirkham, R., Dunn, P.A., Kuczewski, A., Moorhead, G., Geronimo, G.D.,
836 Paterson, D.J., Jonge, M.D., Hough, R.M., Lintern, M.J., Howard, D.L., Kappen, P., Cleverley, J.,
837 2010b. The New Maia Detector System: Methods For High Definition Trace Element Imaging Of
838 Natural Material. AIP Conference Proceedings 1221, 9-17.

839 Ryan, W.B.F., Carbotte, S.M., Coplan, S., O'Hara, A., Melkonian, A., Arko, R., Weissel, R.A., Ferrini, V.,
840 Goodwillie, A., Nitcher, F., Bonczkowski, J., Zensky, R., 2009. Global Multi-Resolution Topography
841 (GMRT) synthesis data set. Geochemistry, Geophysics, Geosystems 10.

842 Rybacki, E., Dresen, G., 2004. Deformation mechanism maps for feldspar rocks. Tectonophysics 382,
843 173-187.

844 Schulmann, K., Martelat, J.-E., Ulrich, S., Lexa, O., Štípská, P., Becker, J.K., 2008. Evolution of
845 microstructure and melt topology in partially molten granitic mylonite: Implications for rheology of
846 felsic middle crust. Journal of Geophysical Research: Solid Earth 113.

847 Smith, J., Piazzolo, S., Daczko, N., Evans, L., 2015. The effect of pre-tectonic reaction and annealing
848 extent on behaviour during subsequent deformation: Insights from paired shear zones in the lower
849 crust of Fiordland, New Zealand. *Journal of Metamorphic Geology* 33, 557-670.

850 Stuart, C.A., Daczko, N.R., Piazzolo, S., 2017. Local partial melting of the lower crust triggered by
851 hydration through melt–rock interaction: an example from Fiordland, New Zealand. *Journal of*
852 *Metamorphic Geology* 35, 213-230.

853 Stuart, C.A., Meek, U., Daczko, N.R., Piazzolo, S., Huang, J.X., 2018a. Chemical Signatures of Melt–
854 Rock Interaction in the Root of a Magmatic Arc. *Journal of Petrology* 59, 321-340.

855 Stuart, C.A., Piazzolo, S., Daczko, N.R., 2016. Mass transfer in the lower crust: Evidence for incipient
856 melt assisted flow along grain boundaries in the deep arc granulites of Fiordland, New Zealand.
857 *Geochemistry, Geophysics, Geosystems*, n/a-n/a.

858 Stuart, C.A., Piazzolo, S., Daczko, N.R., 2018b. The recognition of former melt flux through high-strain
859 zones. *Journal of Metamorphic Geology* 0.

860 Svahnberg, H., Piazzolo, S., 2010. The initiation of strain localisation in plagioclase-rich rocks: Insights
861 from detailed microstructural analyses. *Journal of Structural Geology* 32, 1404-1416.

862 Tucholke, B.E., Lin, J., Kleinrock, M.C., 1998. Megamullions and mullion structure defining oceanic
863 metamorphic core complexes on the Mid-Atlantic Ridge. *Journal of Geophysical Research: Solid*
864 *Earth* 103, 9857-9866.

865 Urai, J., Means, W., Lister, G., 1986. Dynamic recrystallization of minerals. *Mineral and Rock*
866 *Deformation: Laboratory Studies: The Paterson Volume*, 161-199.

867 Walte, N.P., Bons, P.D., Passchier, C.W., Koehn, D., 2003. Disequilibrium melt distribution during
868 static recrystallization. *Geology* 31, 1009-1012.

869 White, S., 1976. The effects of strain on the microstructures, fabrics, and deformation mechanisms
870 in quartzites. *Philosophical Transactions of the Royal Society of London A: Mathematical, Physical*
871 *and Engineering Sciences* 283, 69-86.

872 White, S.H., Knipe, R.J., 1978. Transformation- and reaction-enhanced ductility in rocks. Journal of
873 the Geological Society 135, 513-516.

874 Whitney, D.L., Evans, B.W., 2010. Abbreviations for names of rock-forming minerals. American
875 mineralogist 95, 185.

876 Whitney, D.L., Teyssier, C., Rey, P., Buck, W.R., 2013. Continental and oceanic core complexes.
877 Geological Society of America Bulletin 125, 273-298.

878 Wolff, P.E., Koepke, J., Feig, S.T., 2013. The reaction mechanism of fluid-induced partial melting of
879 gabbro in the oceanic crust. European Journal of Mineralogy 25, 279-298.

880

881 Figure 1: Geological context of the studied sample; (a) location of Atlantis Bank and core 735B (Ryan
882 et al., 2009), profile for (b) marked by dashed line; (b) profile across the Atlantis fracture zone and
883 Atlantis Bank showing relative height of the core complex (GMRT Grid Version 3.6); core section
884 (from shipboard core description) showing: (c) dominant rock types, note location of the 20m thick
885 shear zone studied is marked by cross hatching; (d) proportions of secondary plagioclase (2° Pl),
886 recognized as irregularly distributed recrystallisation of primary plagioclase; (e) proportions of
887 secondary hornblende (Hbl), seen as rims on olivine and pyroxene and along pyroxene cleavages; (f)
888 textures and foliations recognized in the core; (g) images typical of the core (IODP reference for core
889 images: <https://tinyurl.com/IODP-735B>), i) showing magmatic texture from 920 metres below
890 seafloor (mbsf), ii) showing a representative core image of the 20m thick shear zone shown in (c) at
891 963 mbsf; location of studied sample is marked on (c) by dashed line at 953.7 mbsf. Note that the
892 whole shown section belongs to base of rock unit X in the core.

893

894 Figure 2. Overview of sample studied depicting main microstructural domains and their
895 characteristics; plane polarized light thin section photomicrograph with locations of other figures,

896 white dashed for Synchrotron data, black dotted for EBSD pole figures, solid white for SEM images,
897 solid black for (b) to (e); (inset) schematic diagram showing domains and foliation orientations; (b)
898 zoom-in showing brown hornblende (Hbl) in strain shadows on diopside (Di); (c) zoom-in showing
899 enstatite (En) and magnetite (Mag) development on rim of olivine (Ol); (d) zoom-in showing small
900 grain size and phase mixing of diopside, enstatite, brown hornblende and magnetite; (e) zoom-in
901 showing late green hornblende vein; mineral abbreviations are following Whitney and Evans (2010),
902 Pl = plagioclase.

903

904 Figure 3: Mineral chemistry and its relationship to microstructural features; note all hornblende
905 analyses refer to brown hornblende as described in text and Fig. 2. (a) Synchrotron Ca map,
906 equivalent colours for electron microprobe X_{An} calculations are shown here and also in (c); (b)
907 photomicrograph of equivalent area from (a) in crossed polarised light, showing original igneous (Ig)
908 Pl, Pl recrystallized in S_{1a} , S_{1b} and S_2 . Edge of S_2 domain is shown (depicted by yellow dotted line and
909 arrows). Areas of S_{1a} igneous plagioclase and S_{1b} recrystallised plagioclase are outlined in yellow
910 dashed lines. An example of deformation twinning is shown in the zoomed in micrograph (lower
911 right corner; field of view 0.5 mm); (c) plagioclase composition histogram of electron microprobe X_{An}
912 calculations using same key as (a); (d) electron microprobe X_{Mg} calculations for igneous Ol (blue
913 squares) and Di (blue diamonds) overlap with S_{1a} recrystallised Ol and Di (green squares and orange
914 diamonds, respectively); S_{1b} reaction products of En and Hbl after Ol (green triangles and circles
915 respectively) and after Di (orange triangles and circles respectively) are distinct; S_2 reaction products
916 (red symbols) partially overlap S_{1b} data; insets to the right of (d) show context plain polarised images
917 (areas in indicated in (b) by white dashed boxes) with typical locations for each symbol.

918

919 Figure 4: Characteristics of S_{1a} based on EBSD analysis highlighting solid state deformation features
920 such as dynamic recrystallisation of (a) olivine, (b) diopside, (c) plagioclase. 10° grain boundaries
921 marked in black, 2° subgrain boundaries marked in white. Pole figures show data of grains less than
922 $200\ \mu\text{m}$ diameter, one point per grain in grey shades, overlaid by all points for data of grains greater
923 than $200\ \mu\text{m}$ diameter marked in the same colour as the map. In (a) for olivine and (c) for plagioclase
924 the change in orientation from a reference orientation (marked with a white cross) is shown.

925

926 Figure 5. Characteristics of S_{1b} based on EBSD analysis highlighting melt-mineral reactions (a) for Ol,
927 (b) for Di. Misorientation profiles from locations marked with yellow dot and dashed line;
928 background colours show mineral phases; black lines within profiles depict relative orientation
929 change to the profiles' starting point (marked with yellow dot), red lines depict relative orientation
930 change to the neighbours. Note: En and Hbl reaction products are fine grained and display epitaxy
931 relative to the precursor Igneous or S_{1a} Ol and Di orientation. All pole figures are 1 point per grain.
932 Colour scheme shown on (a) and (b) are the same as in Figure 4; 10° grain boundaries are black, 2°
933 subgrain boundaries are white.

934

935 Figure 6. Microstructures indicative of the former presence of melt; back-scattered electron (BSE)
936 images of S_{1b} and S_2 melt-rock interaction microstructures; (a) to (c) S_{1b} , (d) to (f) S_2 . Arrows point to
937 microstructures: red – mineral films along grain boundaries inferred to have pseudomorphed melt,
938 black - low dihedral angles, white – embayments, green – intergrowths. (d) pole figures for central
939 hornblende grain shows that the grain has some crystal faces; note the correlation between colour
940 of crystal planes marked in the pole figure and those in the BSE image. (e) & (f) are the same area of
941 the S_2 domain showing grains connected in 3D (ilmenite grains are numbered Ilm1 to 5); ilmenite
942 grains can be differentiated by their orientations (from EBSD data), where the same colour signifies

943 the same crystallographic orientation and a likely single crystal connected in 3D; colours are
944 repeated on pole figure showing clustering of the different ilmenite orientations; data is presented
945 by overlaying EBSD data onto the greyscale EBSD derived band contrast image in (f).

946

947 Figure 7. Characteristics of S_2 based on EBSD analysis highlighting (a) reaction product minerals
948 showing fine grain sizes, and random orientations in (b) pole figures. Misorientation profiles from
949 locations marked with yellow dot and dashed line; background colours show mineral; black lines
950 within profiles depict relative orientation change to the profiles' starting point (marked with yellow
951 dot), red lines depict relative orientation change to the neighbours. Note: all minerals are fine
952 grained with no internal orientation change in diopside, hornblende and plagioclase grains, while the
953 larger enstatite grains show some orientation change suggesting the latter are residual from S_{1b} ;
954 background colours as related to mineral phases. Pole figures show all grains in the respective map
955 area shown with one point per grain plotted. Colour scheme shown on (a) and (b) are the same as in
956 Figure 4; 10° grain boundaries are black, 2° subgrain boundaries are white.

957

958 Figure 8. Representative temperatures for deformation of the 735B core. M&H 2008 = Mehl and
959 Hirth (2008), B&K 1990 = [Brey and Köhler \(1990\)](#), Putirika 2016 = Putirika (2016), R&R 2012 = [Ridolfi
960 and Renzulli \(2012\)](#); * indicates Brey and Köhler (1990) two pyroxene thermometer. Note that
961 temperatures for S_{1a} (solid state deformation) are lower than for S_{1b} (820–970°C) and S_2 (750–900°C)
962 both of which are inferred to have formed in the presence of melt. The En and Hbl temperatures
963 reflect that of products from the melt-host reactions. We interpret this as the matrix temperature
964 gradually reducing, while multiple influxes of hot melt caused the formation of En and Hbl, possibly
965 at temperatures hotter than the matrix. Between the melt influx events, the temperature of the
966 melt gradually equilibrated with the matrix.

967

968 Figure 9. Summary of different deformation environments recorded in the analysed section. (a) S_0 :
969 Magmatic foliation showing euhedral grains (1) aligned in the magmatic flow (2); sketch based on
970 micrograph image of Deans and Yoshinobu (2019). (b) S_{1a} : Solid state deformation showing large
971 porphyroclasts of anhedral plagioclase (1) with fine grained recrystallized plagioclase in strain
972 shadows (2); sketch based on micrography shown in Figure 4c. (c) S_{1b} : Melt present deformation
973 identified by the presence microstructures indicative of the former presence of melt including
974 asymmetric new mineral growth (1), embayments into original minerals (2), pseudomorphed melt
975 films (3) and low dihedral angles of new minerals after crystallisation of the melt (4); note that there
976 is a significant replacement of original S_0 and S_{1a} minerals marked by #) by minerals associated with
977 melt-rock interaction (En, oxides marked by asterix); sketch based on micrography shown in Figure
978 3b. (d) S_2 : High strain melt present deformation with high melt flux resulting in microstructures
979 typical for melt present deformation as shown in (c) (not shown in sketch), near complete
980 replacement of original S_0 and S_{1a} minerals by minerals associated with melt-rock interaction (En,
981 Hbl, oxides marked by asterix in legend) and phase mixing; see text for details. Abbreviations:
982 GSR_disloc - dislocation creep related grain size reduction, GSR_react – melt reaction related grain
983 size reduction, GBS – grain boundary sliding, GBS_melt – melt assisted grain boundary sliding.

984

985 Table 1. Representative EMP mineral data.